

KINEMATICS OF THE GALACTIC BUBBLE RCW 120

M. Sánchez-Cruces,¹ A. Castellanos-Ramírez,² M. Rosado,³ A.
Rodríguez-González,² and J. Reyes-Iturbide⁴

Draft version: June 5, 2018

RESUMEN

Presentamos el estudio cinemático en las líneas de [SII] $\lambda\lambda 6717, 6731$ Å de la burbuja Galáctica RCW 120. Determinamos que la velocidad radial de esta burbuja se encuentra entre ~ 74 to ~ 6 km s⁻¹. Encontramos evidencia de expansión únicamente en la parte noreste de la nebulosa (de 20 a 30 km s⁻¹). Encontramos alta densidad en la parte suroeste de la nebulosa (4000 cm⁻³) así como dos gradientes de densidad en la parte sur. Con la finalidad de explorar la dinámica, morfología y emisión óptica de RCW 120 presentamos simulaciones numéricas en 3D de esta burbuja usando el código WALICXE-3D. Los resultados numéricos predicen que en promedio la densidad del medio (en la parte sur del objeto) es de entre 3000 to 5000 cm⁻³, lo que concuerda con los valores observados. Los modelos no predicen emisión en rayos X provenientes del cascarón debido a la velocidad de expansión baja.

ABSTRACT

We studied the kinematics of the Galactic bubble RCW 120 in the [SII] $\lambda\lambda 6717, 6731$ Å lines. We measured a LSR radial velocity ranging from ~ 74 to ~ 6 km s⁻¹. We found evidence of expansion only in the northeast region of the nebula (from 20 to 30 km s⁻¹). We found a high electron density around 4000 cm⁻³ in the south-west region and we also found two arches-like structure indicating a density gradient. We present 3D numerical simulations of RCW 120 using WALICXE-3D code in order to explore optical shell dynamics and its morphology. Our numerical results predict an average numerical electron density of the ambient medium (in the southern region of the object) is between 3000 to 5000 cm⁻³ in agreement with our values obtained from the observations. From our models, we do not expect X-ray emission coming from the external shell, due to the low expansion velocity value.

Key Words: H II regions — ISM: individual objects (RCW120)

1. INTRODUCTION

Massive stars ($\gtrsim 25 M_{\odot}$) during their lives inject mechanical energy into the interstellar medium through their stellar winds (with a wind terminal velocity

¹Escuela Superior de Física y Matemáticas, Instituto Politécnico Nacional

²Instituto de Ciencias Nucleares, Universidad Nacional Autónoma de México

³Instituto de Astronomía, Universidad Nacional Autónoma de México

⁴División de Mecánica. Tecnológico de Estudios Superiores de Tianguistenco, Estado de México, México

$v_w=2000 \text{ km s}^{-1}$ and mass loss rate of $\dot{M} \approx 10^{-6}$ to $10^{-5} M_\odot \text{ yr}^{-1}$; e.g. (Friend & Abbott 1986)). The stellar winds could sweep up the interstellar medium creating a dense shell filled with very hot gas known as wind bubble with a few 10 pc of size and superbubbles with sizes ~ 100 pc in case of shell created by stellar winds of star associations. During the evolution of this bubble, the transfer of energy into the interstellar medium (ISM) can be carried out by radiative luminosity (L_*) and by mechanical luminosity due to winds ($L_w = \dot{M}v_w^2$).

The wind bubble formation around this stars begins when the massive star will first have formed an H II region in a very high density with sizes of about 1 pc. During their main sequence and WR phases, the expansion of the ionized gas is driven by the hot shock stellar wind bubble.

In general the H II regions have spherical geometry in a homogeneous density medium, nevertheless some present asymmetric geometric when they are in inhomogeneous medium. This asymmetries can be classified according to their morphology: I) bow shocks of an ionizing star moving supersonically through a molecular cloud (Van Buren et al. 1990; MacLow et al. 1991). II) “Champagne flow” where it is assumed that the massive star is born in a medium with density gradients (Tenorio-Tagle 1979). III) bipolar morphology resulting from the confinement of the ionized gas by a flattened structure of neutral gas and dust (Campbell 1984; Rodriguez et al. 1988).

A bubble created by a massive stars can be explained by the classical H II region. One scenario indicates that the creation of bubbles is driven by the pressure difference between the ambient ISM and the ionized gas of the H II region. The analytical approximation to the expansion of an H II region in an homogeneous ambient medium and does not consider the stellar winds is given by (Spitzer 1978). A second scenario is the H II region expansion in presence of a stellar wind in an uniform medium (Dyson & Williams 1980). An example of the first case is presented by Martins et al. (2010). They found that for the bubble RCW 79, the mechanical wind luminosity is about 10^{-3} its ionizing luminosity in the RCW 79 nebula indicating that the formation of the ring nebula could be attributed to the radiation pressure of the star. So that is in discussion the importance that the stellar winds of massive stars in the formation of the bubbles and superbubbles.

On the other hand, the standard model of Weaver et al. (1977) and Chu & Mac Low (1990) describes these bubbles as extended bubble structures of shock-heated gas emitting X-rays surrounded by a shell of swept-up and cool ISM observed in optical emission. This model considered two shocks: The principal shock of swept-up ISM compressing in a thin shell to temperature about 10^4 K and a secondary shock of heated gas to temperatures 10^6 - 10^7 K.

Considering this last scenery, it is to be expected that around massive stars observed a ring nebula. However, in the optical survey of Wolf-Rayet ring nebulae (Heckathorn et al. 1982; Chu et al. 1983; Miller & Chu 1993; Marston et al. 1994) shows that only $\frac{1}{4}$ from ~ 150 observed Galactic Wolf-Rayet are associated with a ring-like nebulae (Wrigge et al. 2005). Also, in a recently

work, [Chu \(2008\)](#) and [Chu \(2016\)](#) analyzed an HST observations of the H II region N11B (around an OB association LH10). The HST images of this H II region do not show visible ring-like morphological features, however the log slit spectrogram of [N II] $\lambda 6583$ line shows splitting, indicating the existence of expanding shell of size of ~ 15 pc and V_{exp} of $15\text{-}20$ km s $^{-1}$. The conclusion of ([Chu 2016](#)) is that the expansion velocity is associated with weak shocks within the photoionized medium. This medium does not produce an enough density jump to form a bright shell. If the medium is neutral, then there is a density contrast due to the strong shock, and is more easily to observe a ring nebula in HI emission than in optical.

Regarding the X-ray emission of superbubbles, is important take into account that the original work of [Weaver et al. \(1977\)](#) overestimated the observed X-ray luminosity in some bubbles. And for example, others studies like [Harper-Clark & Murray \(2009\)](#) and [Rogers & Pittard \(2014\)](#) underestimate the X-ray emission (see ([Castellanos-Ramírez et al. 2015](#)) for more information). Therefore, from a theoretical point of view, the X-ray luminosity in a bubble is expected. And, seem to exist a correlation between the kinematic of the bubble and X-ray and optical emission.

The study of the kinematics and X-ray emission of the superbubbles presented by [Oey \(1996\)](#) it is proposed two superbubble categories in terms of dynamical data: high-velocity superbubbles and low-velocity superbubbles, the latter type being more consistent with the standard model, for high velocity is proposed an additional source of energy as a supernova explosion ([Rodríguez-González et al. 2011](#)).

Also, X-rays observations from superbubbles N70 and N185 located in the Large Magallanic Cloud (ideal laboratory to observe objects in X-rays by their low extinction), show X-rays emission inside the optical shell ([Reyes-Iturbide et al. 2014](#); [Zhang et al. 2014](#)) and present an excess of X-ray emission. Therefore, to explain the shell formation and the excess of X-ray emission [Rodríguez-González et al. \(2011\)](#) and [Reyes-Iturbide et al. \(2014\)](#) included an additional source of energy to explain them.

On the other hand, NGC 6888 is the only bubble in our Galaxy that has been observed in optical and X-ray emission ([Gruendl et al. 2000](#); [Moore et al. 2000](#); [Toalá et al. 2016](#)), but the distribution of the X-ray emission could be described as filamentary, opposed to the center filled appearance expected in the analytic model.

In this work we address the problem of the correlation between kinematics and X-rays emission in the bubble RCW 120 by using observations in the optical from the Fabry-Perot interferometer PUMA and X-ray data from CHANDRA, assisting us with hydrodynamic numerical simulations.

1.1. RCW 120

RCW 120 is a Galactic Bubble located at 1.3 kpc from the Sun ([Zavagno et al. 2007](#)) bounded by a massive, dense shell with mass $M_{sh} \approx 1200\text{-}2100 M_{\odot}$ ([Deharveng et al. 2009](#)). It is also called Sh 2-3 or Gum 58 and has a

diameter of 1.9 pc (Anderson et al. 2015). The ionizing star of RCW 120, CD-38°11636 or LSS 3959 is an O8 type star (Georgelin & Georgelin 1970; Avedisova & Kondratenko 1984; Russeil 2003; Zavagno et al. 2007) located at $\alpha_{J200}=17^h12^m20.6^s$, $\delta_{J200}=-38^\circ29'26''$. Its magnitude in different filters is $B=11.93$ and $V=10.79$ (Avedisova & Kondratenko 1984), with $M_\star \approx 30 M_\odot$. K-band images of the ionizing star of RCW 120 from 2MASS and SINFONI suggest that the star is double being the companion of the same spectral type (Martins et al. 2010). Table 1 summarize the characteristics and properties of RCW 120.

Current studies carried out with the NANTEN2, Mopra, and ASTE telescopes reveal two molecular clouds associated with RCW 120 with a velocity separation of 20 km s^{-1} (Torii et al. 2015). The cloud at -28 km s^{-1} is distributed just outside the opening ring while the cloud at -8 km s^{-1} traces the infrared ring (Anderson et al. 2015). $\text{H}\alpha$ Fabry-Perot observations of RCW 120 has been done with the survey CIGALE of the Milky Way and the Magellanic Clouds (Le Coarer et al. 1993) on a 36-cm telescope (La Silla, ESO) by Zavagno et al. (2007). These authors found a LSR radial velocity of ionized gas ranges -8 to -15 km s^{-1} and they did not find evidence for expansion of the ionized hydrogen associated with RCW 120.

RCW 120 is possible a triggered star formation region (i.e. like RCW 82, RCW 79) embedded in a molecular cloud (Zavagno et al. 2007). 2MASS, Spitzer and Herschel observations of this bubble reveal the existence of young stellar objects located in the massive condensation in the bubble surrounding (Deharveng et al. 2009; Zavagno et al. 2010) indicating active star formation in the region. Since there should be shock compression triggering the star formation, we obtained Fabry-Perot data at $[\text{SII}]\lambda\lambda 6717, 6731 \text{ \AA}$ because it is easier to identify shocks in [SII] rather than in $\text{H}\alpha$, both because of the higher [SII]/ $\text{H}\alpha$ line-ratio and also because [SII] velocity profiles of each velocity component are narrower than $\text{H}\alpha$ velocity profiles because of larger atomic weight of [SII] relative to the $\text{H}\alpha$.

The layout of the paper is as follows. The observations and data reductions using the Fabry-Perot interferometer are presented in section 2. In section 3 we present the analysis of the kinematics of RCW 120 as well as the morphology and density spatial distribution of this nebula into the ISM. In section 4 we show the numerical evolution of the X-ray emission and shell dynamics of bubble with the physical characteristics of RCW 120. The discussion and conclusions are presented in section 5.

2. OPTICAL OBSERVATIONS AND DATA REDUCTIONS

The observations were carried out in July 2014 using the 2.1 m telescope of the Observatorio Astronómico Nacional of the Universidad Nacional Autónoma de México (OAN, UNAM), at San Pedro Mártir, B. C., México. We used the UNAM scanning Fabry-Perot interferometer PUMA (Rosado et al. 1995). We used a 2048×2048 Marconi2 CCD detector with a binning factor of 4 resulting

in a FoV of $10'$ and dimensions of 512×512 pixels with a spatial sampling of $1''.3 \text{ pixel}^{-1}$.

We obtained [SII] $\lambda\lambda 6717, 6731 \text{ \AA}$ Fabry-Perot data cubes of RCW 120. The Fabry-Perot interferometer has a finesse of ~ 24 leading to a sampling spectral resolution of 0.41 \AA (equivalent to a sampling velocity resolution of 19.0 km s^{-1} at 6717 \AA) and a free spectral range of 20 \AA (equivalent to a velocity range of 929 km s^{-1} at 6717 \AA). The spectral resolution was achieved by scanning the interferometer free spectral range through 48 different channels producing velocity cubes of $512 \times 512 \times 48$ (Rosado et al. 1995). The interference filter used was centered on 6721 \AA with a bandpass of 20 \AA . For calibrating the [SII] cube we used a Neon lamp (6717.04 \AA wavelength calibration) and the calibration data cube has dimensions of $512 \times 512 \times 48$. We also obtained a set of direct images in $H\alpha$ and [SII] using PUMA in its direct imaging mode (see Figure 1). The exposure time of each of the direct images was 120 s. Observational and instrumental parameters are listed in Table 2.

The images were reduced using standard IRAF¹ routines. The data reduction and analysis of the Fabry-Perot data cubes were performed using the CIGALE software. CIGALE allows flat fielding correction, wavelength calibration, construction of velocity maps and derivation of radial velocities, identification of sky-lines, profile extraction and fitting. In this case the data cubes in the [SII] lines are not contaminated by line-sky emission. In the spectral window, the data cubes do not show any sky lines. No spatial or spectral smoothing was applied to the data. The CIGALE data reduction process allows compute the parabolic phase map from the calibration cube. This map provides the reference wavelength for the line profile observed inside each pixel. Also, we can compute from the phase map, the wavelength, monochromatic, continuum maps.

The extraction of the kinematic information from the Fabry-Perot data cube was done using the radial velocity map of RCW 120. This map was obtained using the barycenter of the [SII] $\lambda 6717 \text{ \AA}$ (using as the rest λ) velocity profile at each pixel. The radial velocity profiles were fitted by the minimum number of Gaussian functions after deconvolution by the instrumental function (an Airy function). The result of this convolution is visually matched to the observed profile. The computed width of the Gaussian functions is taken as the velocity dispersion (of the velocity component corrected by instrumental function with a width of 38 km s^{-1}).

3. DATA ANALYSIS

Figure 1 shows the direct images of $H\alpha$ and [SII] $\lambda\lambda 6717, 6731 \text{ \AA}$ emission-lines obtained with PUMA. The ionizing star is marked with a white arrow. We can see a well defined ionization front (IF) of RCW 120 located in the southern region of the nebula showing a section of shell formed with dense material

¹IRAF is distributed by National Optical Astronomy Observatory, operated by the Association of Universities for Research in Astronomic, Inc., under cooperative agreement with the National Science Foundation.

(shocked gas emitting in [SII] emission lines). This region corresponds to the dust condensations #1 and #7 (see [Deharveng et al. 2009](#)) where more Young Stellar Object (YSO) are located. In the opposite side of the IF it is observed an open structure.

3.1. Kinematics of the Nebula

Our Fabry-Perot data allow us to identify the global trends of the kinematics of RCW 120 in [SII] emission. With the Fabry-Perot interferometer PUMA it is possible to study both the large scale motions and the punctual motions like expansion velocities unlike the classical long-slit spectrometers which is limited by the aperture spectrometry giving information of a small part of the object.

Figure 2 shows a mosaic obtained with the observed fields with the [SII] radial velocity profiles integrated over windows of 20×20 pixels size ($26'' \times 26''$) overlaid in a [SII] image. The x and y axis indicates the (x,y) position of each integrated velocity profile. In this figure we can see that the brightest emission is coming from the southern region of nebula, the two [SII] $\lambda\lambda 6717, 6731$ Å lines are detected and are separated by about 15 channels (equivalent to 285 km s^{-1}). Profiles from the northern region show different intensities between the two [SII] lines, whereas the profiles from the southern region seem to have the same intensity. Since both lines $\lambda 6717$ Å and $\lambda 6731$ Å are emitted by the same gas, we will focus on the brighter line ([SII] $\lambda 6717$ Å).

We have fitted the velocity profiles shown in Figure 2 using Gaussian functions and considering those with a significant signal to noise and taking into account the brighter line ([SII] $\lambda 6717$ Å). We corrected the observed FWHM to account for effects that broaden the lines. The instrumental broadening σ_{inst} has been done in the deconvolution of the Airy function and in this case correspond to 38 km s^{-1} . We computed the thermal broadening according to $\sigma_{th} = \sqrt{82.5(T_4/A)}$ where $T_4 = T/10^4$ K and A is the atomic weight of the atom. The correction for thermal broadening to the [SII] is about 1.6 km s^{-1} ($A_{sulfur} = 32.065 \text{ u}$), compared with the instrumental broadening this has no effect upon our results. The fine structure of atoms broadening correction σ_{th} is important for hydrogen and helium recombinations lines, but not for metal lines such [SII] and [NII] ([García-Díaz et al. 2008](#)), so this correction is not required. The turbulence broadening σ_{tr} is related other motions like nonthermal motions. Often complicated by superpositions along the line of sight of emission completely independent of the observed structure ([Courtès 1989](#)), therefore the turbulence broadening has no effect upon our conclusions.

From the velocity profile fit we found that the profiles in the northeastern region of the nebula (in the side of the open structure) are complex and broad, indicating the presence of different motions in that region. The profiles in the southern region of the bubble present single broad [SII] profiles corresponding to the radial velocity of the nebula. In the spectral window, the data cubes

do not show any sky lines. No spatial or spectral smoothing was applied to the data.

In Figure 3 we present the spatial distribution of velocity profiles with single component (dark gray) and with double velocity components (light gray). As can be seen in this figure, the regions with two velocity component are located in the northeast side of the nebula (region of the open structure of the nebula) and some in the west side of the nebula.

In order to show the differences between bright components we show in Figure 4 the radial velocity profiles of one region with a single velocity component and other one with two velocity components. The x -axis in the profiles is given in channels (each channel has associated a wavelength) and the y -axis gives the intensity of the line in arbitrary units. The single component of the velocity profiles correspond to the radial velocity of the nebula. In the case of velocity profiles with two components, these are called extreme velocity components. We shall refer to these as V_{main} (represents the radial velocity of the nebula) and V_{sec} (associated with others movements). These are marked with No. 0 and No. 1, respectively.

Figure 5 display the velocity maps of the components obtained from the fit profiles. Top panel shows the velocity map of the V_{main} component. Bottom panel shows the velocity map of the V_{sec} component. The highest LSR velocity values coming from the southeast side of the nebula. The VLSR present a gradient of about $\Delta_{V_{LSR}}=60 \text{ km s}^{-1}$ (varies between -74 km s^{-1} to -6 km s^{-1}). This velocity gradient match with the CO distribution of the red cloud towards this nebula presented by Torii et al. (2015).

The expansion velocity determined for the regions with composite profiles is $V_{exp}=20 \text{ km s}^{-1}$, this value was calculated by using the expression: $V_{exp}=(V_{main}-V_{sec})/2$.

3.2. Emission-line Ratio Maps and Electron Density

Figure 6 shows the [SII]/H α line-ratio map. We can see that the highest values are located in the IF and from the northern region of the nebula showing the gas shocked on this regions. In the west region of the nebula the [SII]/H α values span from 0.2 to 0.3, while on the east region of the nebula, the values span form 0.1 to 0.2. These differences indicate that the ISM is not homogeneous. From Figure 6 we can see that the highest [SII]/H α line-ratio values correspond to the northern region of the nebula where the profiles with highest velocity values are located.

From our [SII] data cube, where both 6717 Å and 6731 Å lines are detected, we were able to compute [SII] λ 6717/[SII] λ 6731 line-ratios (see Figure 7). The line-ratio values span from 0.3 to 1.5. The lowest [SII] λ 6717/[SII] λ 6731 line-ratio values are located inside on the nebula.

In order to explore the morphology of the nebula RCW 120, we obtained the electron density map assuming a constant electron temperature of 10000 K, corresponding to the expected conditions in H II regions, using the [SII] λ 6717/[SII] λ 6731 line-ratio map.

The electron density map was computed using,

$$\frac{I([\text{SII}]\lambda 6717)}{I([\text{SII}]\lambda 6731)} = 1.49 \frac{1 + 3.77x}{1 + 12.8x} \quad (1)$$

where x is defined as $x \equiv 10^{-4} n_e T^{1/2}$ and T is the electron temperature in units of 10^4 K (McCall et al. 1985).

In both cases we do not correct for differential extinction between $\text{H}\alpha$ and $[\text{SII}]$ and the two lines of $[\text{SII}]\lambda\lambda 6717, 6731$ due to this lines are too close each other making the correction not significant.

In the lower panel of Figure 7 we present the electron densities map. We obtained a maximum density of $\sim 3000 \text{ cm}^{-3}$ in the southern region of RCW 120, and we fixed a minimum density of 0.03 cm^{-3} (in order to run out numerical models). Also, from this figure we can see the spatial variation of electron density, n_e , in the southern region of the nebula presents high electronic density ($\sim 3000 \text{ cm}^{-3}$) and it is possible to appreciate two arches-like structures (south-south-west and south-south-east). The external one presents electronic density values between 3 to 400 cm^{-3} ; while the internal arc has values between 3 to 40 cm^{-3} . The presence of two arches-like regions could be due to the difference in density of the clouds where the H II region seems to be evolving as proposed by Torii et al. (2015). The lower electronic density values are found in the northern region of the nebula; these differences in density cause a faster expanding material in this region allowing that the ionized gas could break the shell. This is known as the ‘‘champagne phase’’ (Tenorio-Tagle 1979).

4. CHANDRA X-RAY OBSERVATIONS AND GAS DYNAMIC SIMULATION OF RCW 120

Given the characteristics of the ionizing star of RCW 120, it is expected that this bubble presents X-ray emission. In order to study their emission at these wavelengths, we obtained the X-ray data of RCW 120 from the Chandra data archive. It has been observed with the Chandra X-Ray Observatory on 2012 June 30 and July 1 Chandra ObsID 13621 using the Advanced CCD Imaging Spectrometer (ASIS) with an exposure time of 49 ks. We reprocessed level 2 data with *chandra-repro* and filtering out periods of high background using *lc-clean*, left a total exposure of 39.7 ks. We used Chandra Interactive Analysis of Observations (CIAO) version 4.7 to analyze the X-ray data using calibration data from CALDB version 4.6.8. A preliminary inspection of the images obtained does not reveal significant diffuse X-ray emission within the nebula. Several point sources have been identified, even though there is no detection of diffuse X-ray emission coming from this bubble.

In order to explore the X-ray emission and the shell dynamics of the RCW 120, we developed 3D numerical gas dynamics simulations. In this case we do not include photoionization nor radiation pressure because we have considered that even though massive stars form around of an H II region

before the effect of its powerful wind interact with the surrounding medium (ionized gas), it is not entirely clear when one effect dominates over the other. As we mention above, in some cases, the creation of bubbles is simply driven by the pressure difference between the ambient ISM and the ionized gas of the H II region, and the effect of mechanical energy due to stellar wind is negligible.

Also, [Mackey et al. \(2016\)](#) compared synthetic infrared intensity maps made by numerical simulations with some Herschel infrared observations for RCW 120. They conclude that, in order to obtain the shape and size of an brightly arc in the infrared waveband, they have to include stellar winds in their simulations.

On the other hand, [Martins et al. \(2010\)](#) point out that the dust emission in 24 μm (the same wavelength used in [Mackey et al. 2016](#)) does not completely favor a strong influence of stellar winds.

Recently, [Gvaramadze et al. \(2017\)](#) reported both, observations and numerical simulations of an H II region IRAS 18153-1651. They found an optical arc near to the centre of the nebula, and suggest that this arc is the edge of a wind bubble together with the H II region produced by a B star. They validated their hypothesis with analytical calculations of both, the radius of the bubble and that of the H II region which fit with the observations. Also, they obtained synthetic $\text{H}\alpha$ and 24 μm dust from 2D numerical simulations of radiation hydrodynamics. Their results match in good agreement with the observations, in the case of the morphology and surface brightness.

Therefore, in order to support the use of only stellar wind in our simulations, we follow the work of [Raga et al. \(2012\)](#). They obtained an analytical model for an expanding H II region driven by stellar winds and the ionizing radiations, both of them coming from the central source. The transition between the two phases is related with the λ parameter (see equation (29) in [Raga et al. 2012](#). and equation (26) in [Tinoco-Arenas et al. 2015](#)):

$$\lambda = 63 \left(\frac{\dot{M}}{5 \times 10^{-7} \text{M}_{\odot} \text{yr}^{-1}} \right) \left(\frac{v_w}{2500 \text{km s}^{-1}} \right)^2 \left(\frac{n_a}{10^5 \text{cm}^{-3}} \right)^{1/3} \left(\frac{10^{49} \text{s}^{-1}}{S_*} \right)^{2/3} \left(\frac{1 \text{km s}^{-1}}{c_0} \right)^{1/3} \quad (2)$$

Basically, they conclude that if $\lambda > 1$, then the expansion of the region becomes the model for a wind-driven shell with a negligibly thin H II region.

In such way, we have calculated the λ -parameter in terms of the values used in our numerical simulations (see Table 3), we obtained a $\lambda > 1$. Therefore, in a good approximation, we can only consider the effects of stellar wind in order to study the X-ray emission in our numerical models.

Finally, we perform a set of three different numerical simulations using the WALICXE-3D code (see [Esquivel et al. 2010](#); [Toledo-Roy et al. 2014](#)). This code solves the hydrodynamic equations on a three dimensional Cartesian adaptive mesh using a second-order finite volume conservative Godunov upwind method, with HLLC fluxes [Toro et al. \(1994\)](#) and a piecewise linear reconstruction of the variables at the cell interfaces with a Van Leer slope limiter. Additionally,

the code includes artificial viscosity for the purpose of stabilize the simulation. The energy equation includes the cooling function appropriate for describing the cooling of the shocked wind material. The cooling function, for different metallicities, was obtained from the freely available CHIANTI database (Dere et al. 1997; Landi et al. 2006).

The computational domain is a cube of 5 pc on a side, with an uniform medium of number density n_0 and temperature T_0 (see below). We used 5-levels in the adaptive grid with a maximum resolution of 256 points along each of the x, y and z axes.

Our numerical models considered appropriate values of the stellar wind velocity and mass injection rate for one single O8V star (see Sternberg et al. 2003 & Mackey et al. 2015 for the mass used in the simulation). The star was placed at the center of the box simulation and its stellar wind was imposed in a region of 5 pixels, corresponding to a physical radius of 0.08 pc. In this region we impose a steady-state spherical stellar wind solution with a $\propto R_w^2$ density profile, such that: $\dot{M} = 4\pi\rho V_\infty R_w^{-2}$. Also, the energy injected by the stellar wind must satisfies $E = \rho|\mathbf{u}|^2/2 + P/(\gamma - 1)$, with P the pressure due to the wind. Moreover, in order to improve the steady-state wind, we include a slope in velocity such that $v_\infty \propto R_w^{-1}$.

We explored three values of n_0 , the cloud density, these are: 2000, 3000 and 6000 cm^{-3} . Table 3 shows the initial condition physical properties for the three numerical models, M1, M2 and M3. Column 1 indicates the model. Column 2 shows the wind velocity. Column 3 shows the mass loss rate. Columns 4 and 5 show the is the density and temperature for the surrounding environment. Column 6 shows the luminosity. We used a super-solar metallicity for the wind and a sub-solar metallicity in the interstellar medium, 3 and 0.3 Z_\odot , respectively (see Castellanos-Ramírez et al. 2015). We have carried out time integrations from $t = 0$ up to $t = 0.4$ Myr for all the models.

4.1. Numerical Results

The evolutionary X-ray emission for the models was computed using emission coefficients in the low-density regime taken from CHIANTI data base as function of the metallicity (see Figure 2 in Castellanos-Ramírez et al. 2015) in the band of 0.6 to 10 keV (soft and hard X-ray band). Figure 8 shows the temperature, column densities and intrinsic X-ray emission maps, upper middle and lower panels, respectively, for the models M1, M2 and M3, left, center and right panels, respectively, at $t=400$ kyr. From row density maps, one can see the radius of the shell driven by the stellar wind. As we expect the model M3, a denser interstellar medium, have small shell radius. On the other hand, we can not see a contribution of the X-ray emission coming from the shocked

environment, by the leading shock. This shell, in the case of RCW 120 is highly dense and the expansion velocity is around 20-40 km s⁻¹. The gas, in the post-shock region, has a temperature around tens of thousands kelvins, i.e. with optical emission. Nevertheless, a weak X-ray emission region is predicted in the not shocked wind region, the very low dense gas region (see also the upper panel in Figure 9).

In addition, the time when the models reach their maximum X-ray luminosity value is different from every model, as one would expect. It is about 60 kyr for model M1, 90 kyr for model M2 and 210 kyr for M3. Nevertheless, the intrinsic X-ray emission is about two order of magnitude less than the X-ray emission coming from the central star associated to RCW 120 (as we can see in the lower panels of Figure 8). In this way, the X-ray luminosity in this region has a very low value to be detected.

Therefore, from our numerical simulation we do not expect a detectable X-ray emission coming from the shocked gas of RCW 120 even when the temperature values reach 10⁷ K. Table 4 shows the results for for models M1, M2 and M3. Column 1 shows indicates the model. Columns 2 and 3 show the position and width of the optical shell (the shocked interstellar medium). Columns 4 shows the total soft X-ray luminosities at t=400 kyr and Column 5 shows the maximum value of the soft X-rays luminosity reached by this numerical bubbles in the band: 0.6 to 10 keV.

Notice that the external shell, in our models, do not have X-ray emission despite that the main source of X-ray emission in bubbles is the medium swept up by the front shock. The shock wave rises the temperature of the gas and the maximum temperature, the post-shock temperature, is around 10⁷ K for stellar wind velocities of ~10³ km s⁻¹. In order to see this behavior more clearly, we present the density, temperature and velocity behavior as a function of the radius in Figure 9. We notice, as we mention previously, that the zone of very low density corresponds to high temperature as well as high velocity. When the density increases (upper panel in Figure 9), the other variables go down (middle and lower panels in Figure 9). On the other hand, as we can see from Figure 9 (bottom panel), the numerical value of the velocity obtained from the simulations, ~4 km s⁻¹ for the RCW 120 is in good agreement with the expansion velocity measured from the observational data, which is in the range 20-40 km s⁻¹, at a radius of 1.9 pc.

On the other hand, the density of the external shell is, at least, 4 times larger to the interstellar medium density, for an adiabatic expansion of a supersonic gas. However, the case of bubble evolving into dense ambients, i.e. the maternal cloud, the external shell of this bubble lose an important fraction of their thermal energy because of the radiative processes (cooling). The temperature of the gas, into the outer shell, drops from 10⁷ K to 10⁴ K in a cooling time giving by,

$$t_{cool} = \frac{E_{th}}{L_{rad}} = \frac{nkT/(\gamma - 1)}{n^2\Lambda(Z, T)} = \frac{kT/(\gamma - 1)}{n\Lambda(Z, T)}, \quad (3)$$

where, E_{th} is the thermal energy, L_{rad} is the cooling rate, k is the Boltzman constant, n is the numerical density, T the gas temperature, Z is the metallicity of the gas, and $\Lambda(Z, T)$ is the cooling function as a function of Z and T . We can also re-write the cooling time (for a gas with initial temperature of 10^7 K) as,

$$t_{cool} = 2.5 \times 10^4 \left(\frac{n}{1000} \right)^{-1} [yr] \quad (4)$$

where, the cooling function values were obtained from [Castellanos-Ramírez et al. \(2015\)](#). Using the equation 4 we calculated the cooling time $t = 1.25 \times 10^4$, 8.34×10^3 , and 4.17×10^3 yr, for the models M1, M2 and M3, respectively. Therefore, in the case of RCW 120, we expect that the gas within the external shell keeps at a temperature around tens thousands of kelvins.

Therefore, in order to reproduce the shell size and width, our simulation predicted the average numerical density of the ambient medium (in southern region of the object) between 3000 - 5000 cm^{-3} and an interstellar medium density around 1000 cm^{-3} for the northern region of RCW 120.

5. DISCUSSION AND CONCLUSIONS

We have analyzed the kinematics and the predicted X-ray luminosity of the galactic Bubble RCW 120 using the PUMA Fabry-Perot interferometer and 3D numerical simulations. From the PUMA direct images we found that the $\text{H}\alpha$ and [SII] emission (see Figure 1) show in both cases a diffuse “halo”, but in the [SII] image shows the ionization front in the southern region of the nebula. In both cases the halo is not perfectly symmetric and is more extended toward the northern region of the nebula. We found that the higher [SII]/ $\text{H}\alpha$ ratios are located in the northern region of the nebula.

Kinematic information of RCW 120 in [SII] line emission obtained here reveals that the LSR radial velocity ranges from ~ 74 to ~ 6 km s^{-1} , in agreement with the values derived from $\text{H}\alpha$ by [Zavagno et al. \(2007\)](#). Also, indicates that it may be a champagne phase. Double component profiles are present in the northern region of this nebula. On the southern region of the bubble no expansion velocity has no component; while in the northern region the expansion velocity span 20 to 30 km s^{-1} . This behavior can be related with a complex structure in the interstellar medium where the shell is evolved, i.e., part of this bubble is within its molecular cloud.

We presented a density map obtained from the [SII] $\lambda 6717$ /[SII] $\lambda 6731$ line-ratio emission, and we found a maximum density around 4000 cm^{-3} in few regions of the southern region of RCW 120 region. We also proposed the existence of two arches-like structure in southern region of the nebula emitting in [SII] emission lines. With densities between 3 to 400 cm^{-3} (for the external arc) and between 3 to 40 cm^{-3} (for the internal arc). This is in agreement with the fact that there are two molecular clouds physically associated with RCW 120 with a velocity separation of 20 km s^{-1} ([Torii et al. 2015](#)).

Regarding to X-ray simulations, for all models we considered super-solar metallicity for the wind and a sub-solar metallicity in the interstellar medium, 3 and 0.3 Z_{\odot} , respectively. The mass loss rate is $\dot{M}=2.7\times 10^{-7} M_{\odot} \text{ yr}^{-1}$ evolved at age of 0.4 Myr. We found that Model M2, with a numerical density in a single cloud of 3000 cm^{-3} is the model that best fits the dynamics of the southern region of the bubble. This model predicts a $R_{Shell}=2.12 \text{ pc}$, $\Delta R_{Shell}=0.68 \text{ pc}$ and no X-ray emission is predicted.

Moreover, we have considered an homogeneous density for the three models overlooking the champagne flow show in the case of RCW 120. As far as we know, both in terms of models of H II regions, or of winds of stars, the case of RCW 120 has not been simulated using a champagne flow. We expect this fact certainly reduce the pressure in the bubble (by providing a channel for it to escape), what will produce changes in the density and temperature. Nevertheless, following the morphology of RCW 120, which is almost spherical, we expect this changes are not so relevant and we can speculate that the champagne flow effect is not determinant at all yet for the X-ray emission, at least in the southern region of RWC 120, which is the densest region with the highest temperature, that most contributes to the aforementioned emission.

Finally, according to [Crowther \(2007\)](#), the minimum mass that a star has to be to become a WR star is $\sim 25 M_{\odot}$ (at solar metallicity), that means the stellar mass of the ionizing star in the case of RCW 120 is enough to become a WR star. Therefore, we would expected that in the case of a more massive star, for example a Wolf-Rayet star or a Of star with high stellar winds, we would expected that the expansion velocity of the bubble obtained from the simulations presented in this work, will be higher than that found in RCW 120 with a O8V star. Nevertheless, it is important that taking into account that this effect depends of the medium as discuss in [Chu \(2008\)](#) and [Chu \(2016\)](#).

We acknowledge support from CONACyT grants 253085 and 167625. This work was also supported by DGAPA-UNAM grants PAPIIT-IN103116, IA-103115, IN-109715 and IG-RG-100516.

Mnica S.C. acknowledges CONACYT for a doctoral scholarship.

Based upon observations carried out at the Observatorio Astronómico Nacional on the Sierra San Pedro Mártir (OAN-SPM), Baja California, México.

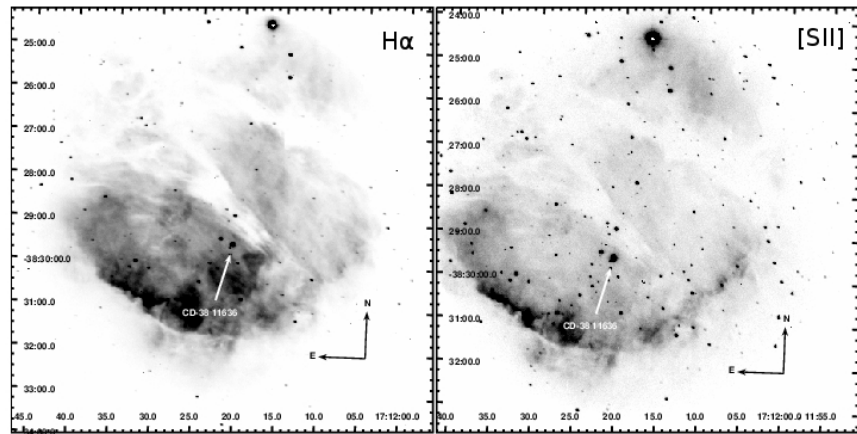


Fig. 1. Direct images of RCW 120, *left panel*: shows the $H\alpha$ emission and *right panel*: shows $[SII]\lambda\lambda 6717, 6731 \text{ \AA}$ emission. We are pointing, with a white arrow, the ionizing star position (Sh2-3).

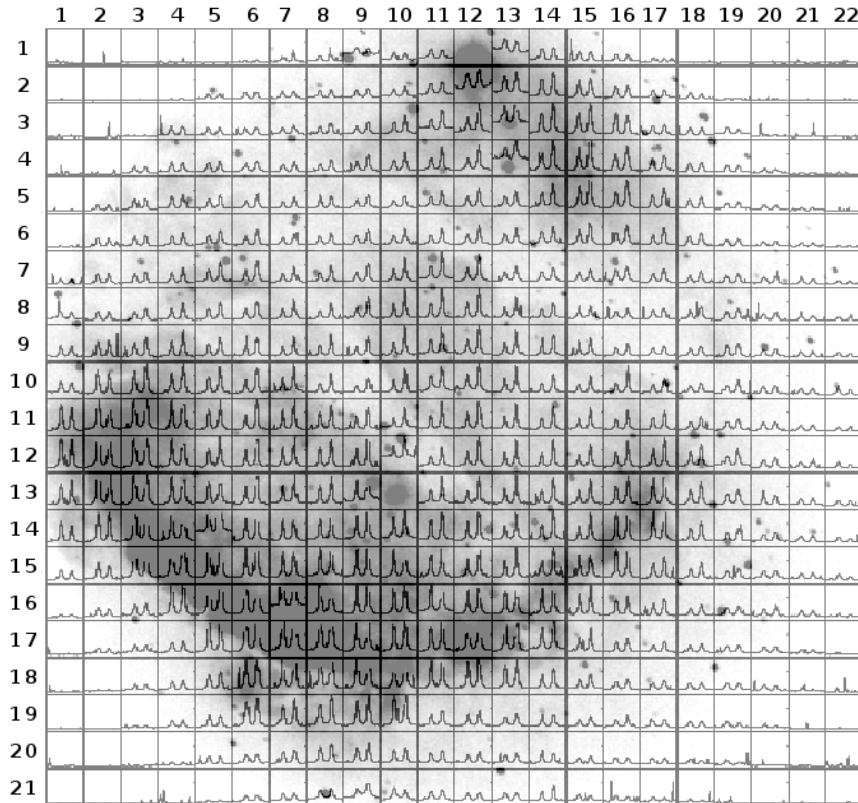


Fig. 2. Some examples of the [SII] radial velocity profiles (20×20 pixels velocity profile plots) of the different regions of RCW 120 superimposed on a [SII] emission velocity map at -21 km s^{-1} (gray color). The numbers in top and left indicate the coordinates of the profiles position.

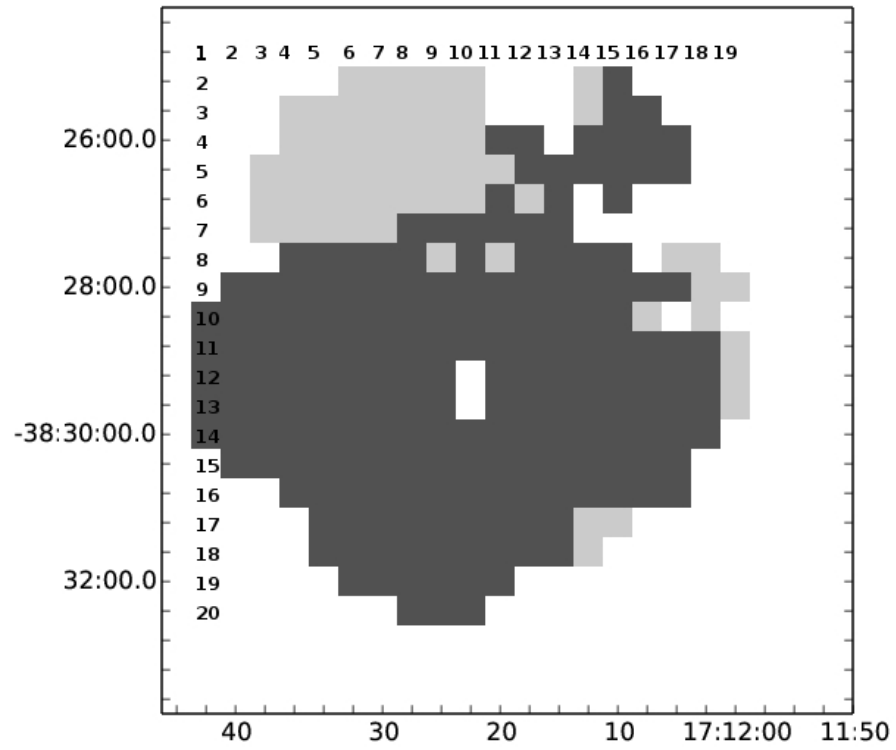


Fig. 3. Spatial distribution of velocity profiles with single and double component. Each region represent the same as in Figure 2 with a size of 20×20 pixels. Profiles with single component are in dark gray and profiles with double velocity components are in light gray.

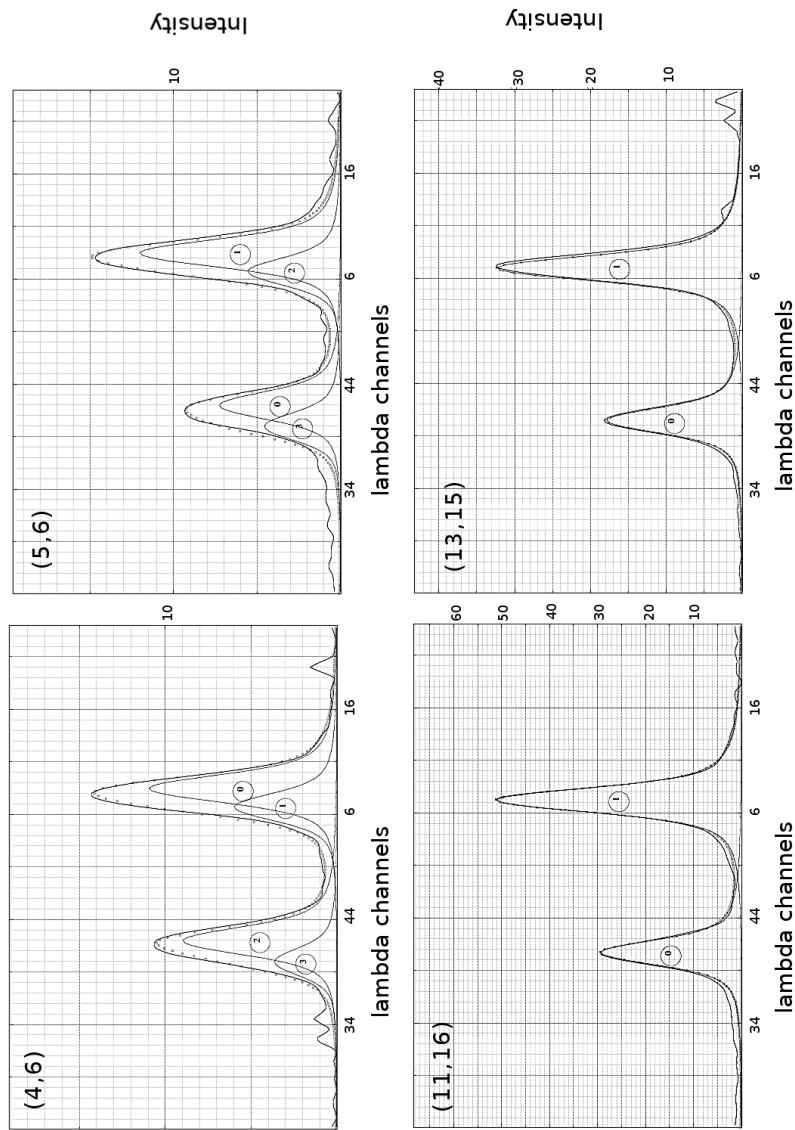


Fig. 4. [SII] radial profiles of four regions obtained with Fabry-Perot. In top-left it is presented the (x,y) position of the extracted integrated velocity profile according to Figure 2. Top profiles are composite, bottom profiles are single. The profiles were integrated over boxes with a 20×20 pixel size. The x-axis in the profiles is given in lambda channels and y-axis is the intensity in arbitrary units. Both [SII] lines at 6717 \AA and 6731 \AA are detected. Decomposition of each profile is indicated in thin lines. Resulting profile is shown as hollow circles and with numbers. Dotted line represent the sum of all fitted components.

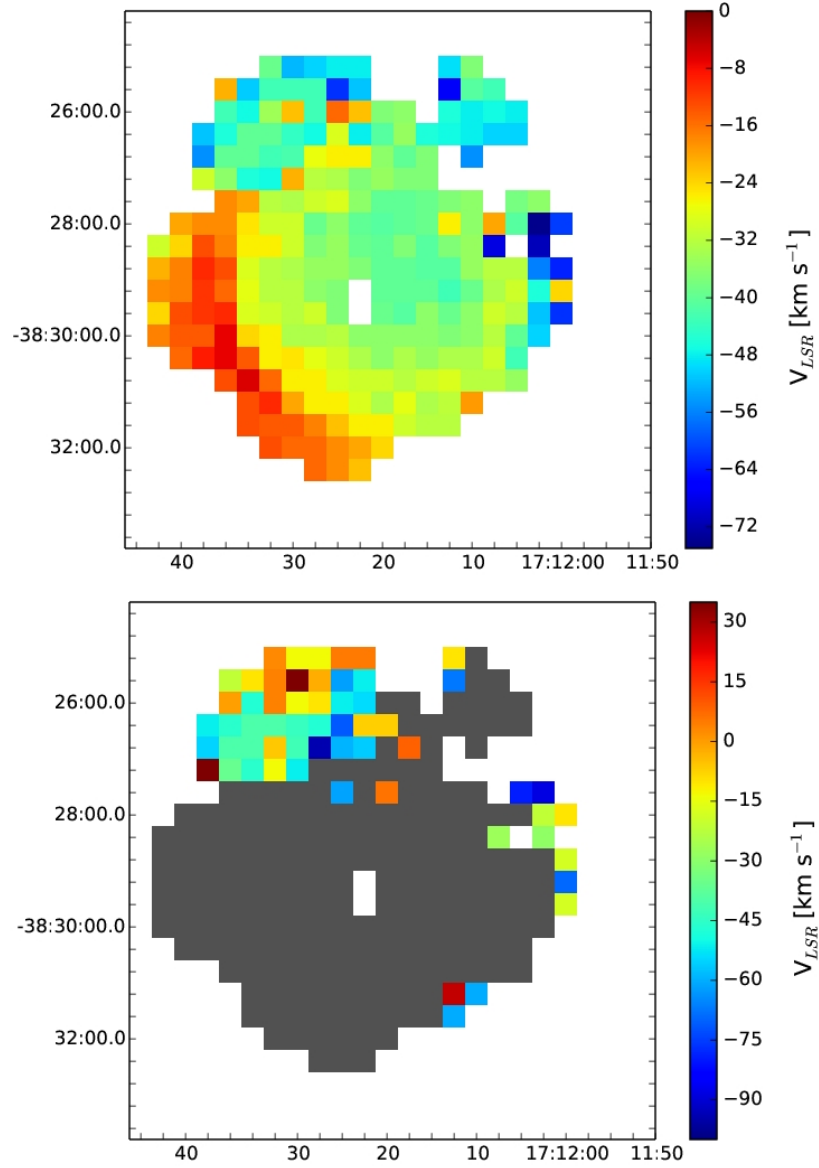


Fig. 5. Velocity maps of the components obtained from the fit profiles. Top panel: velocity map of the V_{main} component. Bottom panel: velocity map of the V_{sec} component. Color gray represents the regions with a single velocity component.

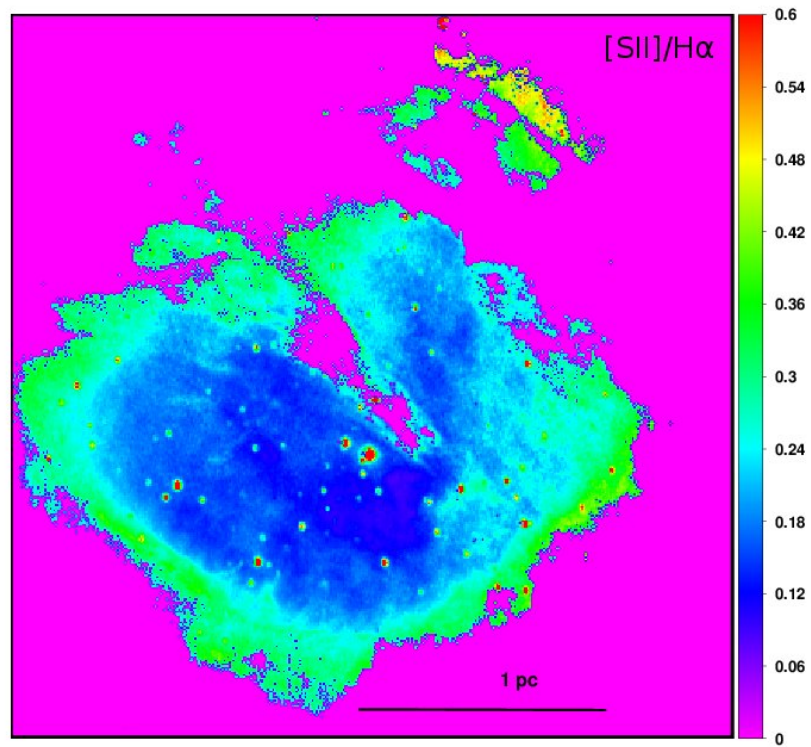


Fig. 6. [SII]/H α line-ratio map. The map is oriented such that north is up and east is to the left.

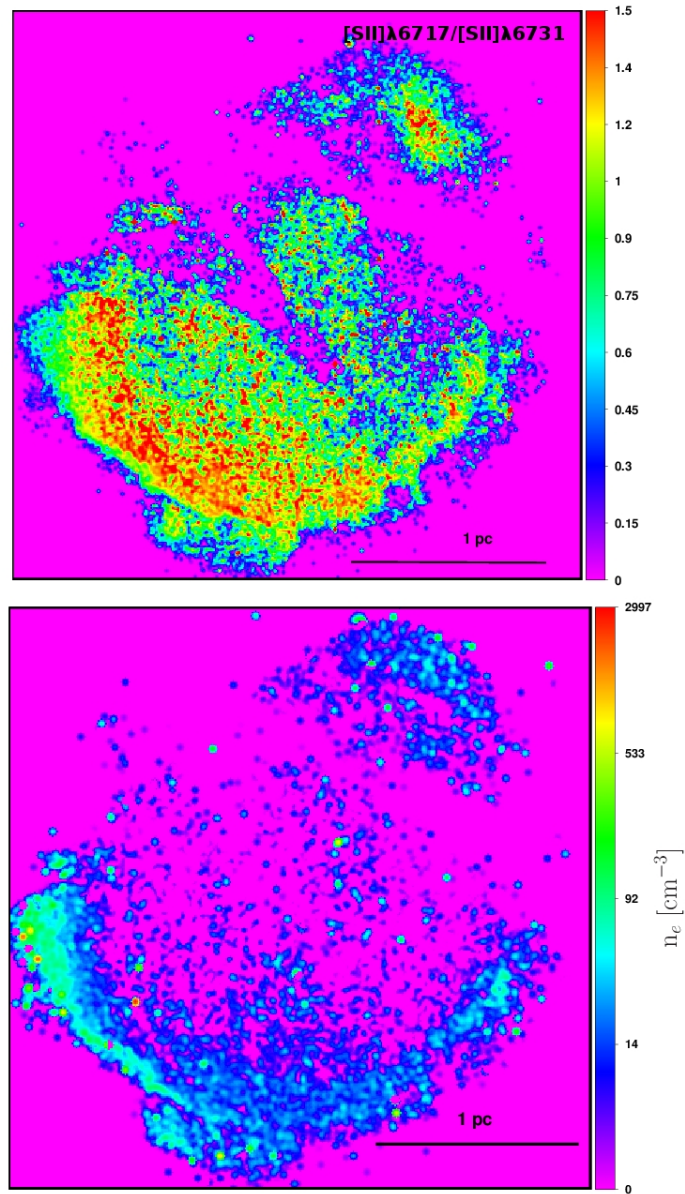


Fig. 7. *Top panel:* $I([\text{SII}] \lambda 6717)/I([\text{SII}] \lambda 6731)$ ratio. *Bottom panel:* Electron density map in particles per cm^{-3} . The maps are oriented such that north is up and east is to the left.

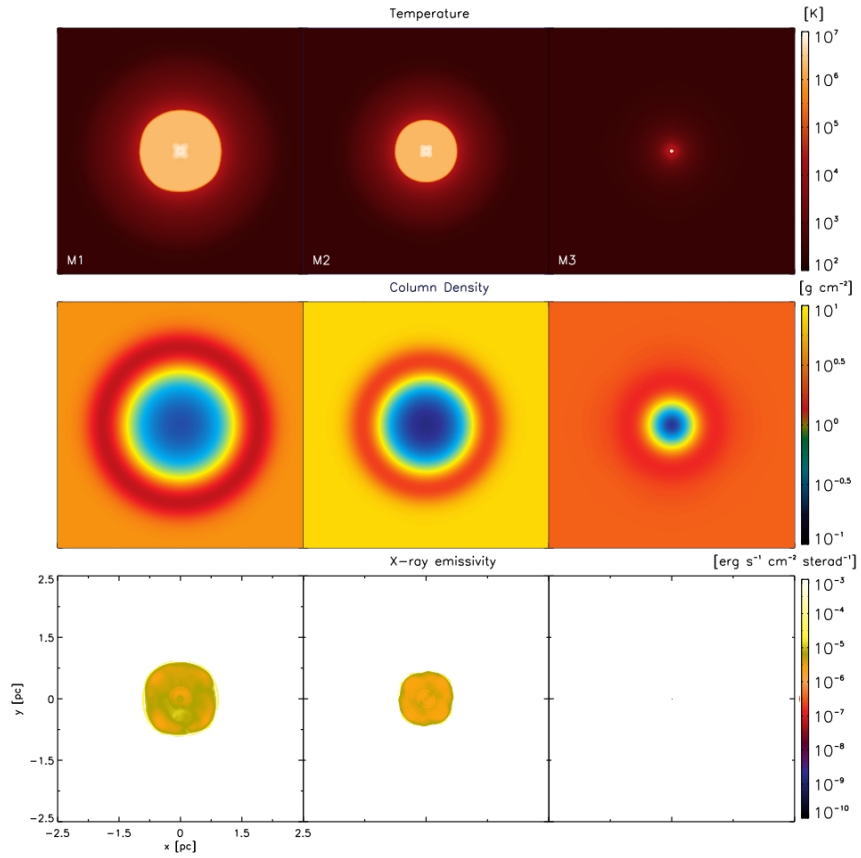


Fig. 8. Temperature, column density and intrinsic X-ray emission maps, upper, middle and lower panels respectively at evolutionary time of 400 kyr. The results of model M1, M2 and M3 are presented.

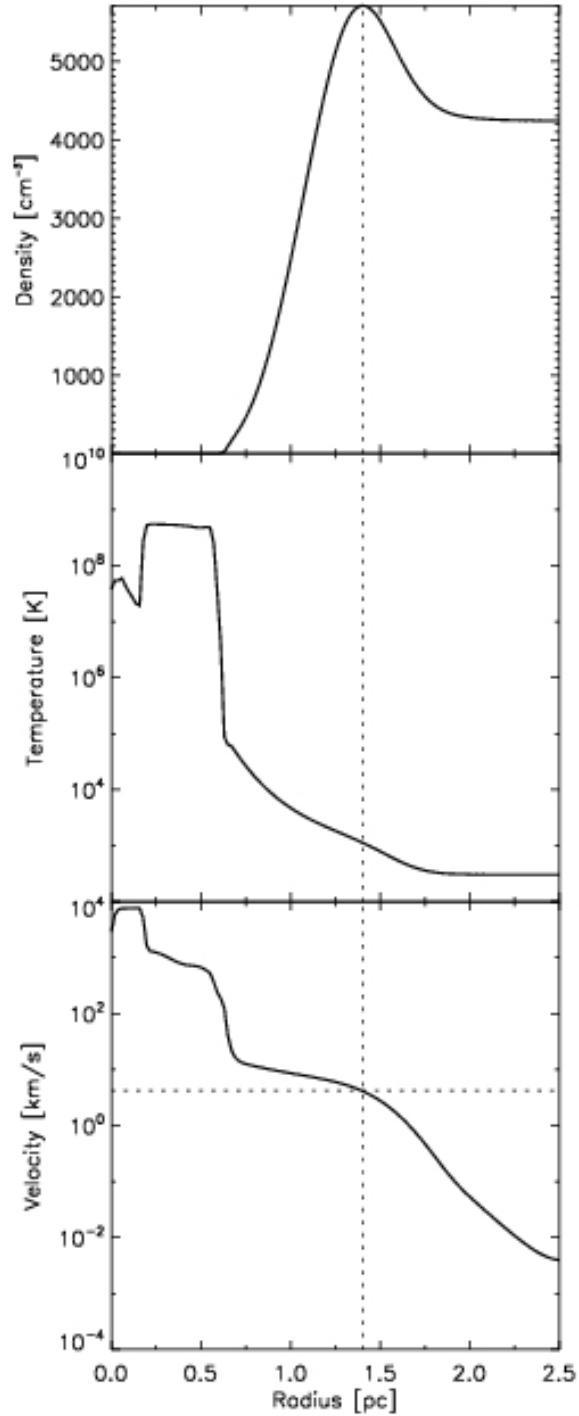


Fig. 9. Density, temperature, and velocity, upper, middle and lower panels respectively. As we explained in the text, the region of higher values for the density (marked with a dotted line) correspond to lower values to temperature and velocity and conversely. Moreover, the velocity value obtained in our numerical simulations ($\sim 4 \text{ km s}^{-1}$) is in agreement with the observational values reported.

TABLE 1
CHARACTERISTIC OF RCW 120 AND ITS IONIZING STAR

Bubble parameters	Value	Reference
Names	Sh2-3	Sharpless (1959)
Distance [kpc]	1.34	Zavagno et al. (2007)
Radius [pc]	1.9	Anderson et al. (2015)
n_0 [cm^{-3}]	2000-6000	Anderson et al. (2015)
$n(\text{H}_2)$ [cm^{-2}]	1.4×10^{22}	Torii et al. (2015)
$n(\text{H}_2)_{\text{ring}}$ [cm^{-2}]	3.22×10^{22}	Torii et al. (2015)
M_{ring} [M_{\odot}]	3100	Torii et al. (2015)
	2000	Deharveng et al. (2009)
$M(\text{H II})$ [M_{\odot}]	54	Zavagno et al. (2007)
r_{ring} [pc]	1.7	Torii et al. (2015)
t [Myr]	0.4	Torii et al. (2015); Zavagno et al. (2007)
ionizing star parameters		
Age [Myr]	5	Martins et al. (2010)
B [mag]	11.93	Avedisova & Kondratenko (1984)
V [mag]	10.79	Avedisova & Kondratenko (1984)
J [mag]	8.01	Avedisova & Kondratenko (1984)
H [mag]	7.78	Martins et al. (2010)
K [mag]	7.52	Martins et al. (2010)
M_* [M_{\odot}]	30	Martins et al. (2010)
$\log(L_*/[L_{\odot}])$	5.07	Martins et al. (2010)
t_{eff} [K]	37500	Martins et al. (2010)
\dot{M} [$M_{\odot} \text{ yr}^{-1}$]	1.55×10^{-7}	Mackey et al. (2015); Martins et al. (2010)
L_0 [erg s^{-1}] ^a	10^{38}	Martins et al. (2010)

^a L_0 is the ionizing photon luminosity

TABLE 2
OBSERVATIONAL AND INSTRUMENTAL PARAMETERS

Parameter	Value
Telescope	2.1m (OAN, SPM)
Instrument	PUMA
Detector	Marconi CCD
Scale plate	0" .33/pix
Binning	4
Detector size [pixels]	2048 × 2048
Central Lambda Å	6720
Bandwidth Å	20
Interference Order Å	322 at 6717 Å
Free spectral range [km s ⁻¹]	929
Exposure time calibration cube	0.5 s/channel
Exposure time object cube	120 s/channel

TABLE 3
INITIAL CONDITIONS OF THE NUMERICAL SIMULATIONS

Model	v_{term} [km s ⁻¹]	\dot{M} [M _⊙ yr ⁻¹]	n_0 [cm ⁻³]	T_0 [K]	Log ₁₀ L_w
M1	2313	2.7×10^{-7}	2000	100	5.4 L _⊙
M2	2313	2.7×10^{-7}	3000	100	5.4 L _⊙
M3	2313	2.7×10^{-7}	6000	100	5.4 L _⊙

TABLE 4
NUMERICAL RESULTS

Model	R_{shell} [pc]	ΔR_{shell} [pc]	L_X [x10 ²⁹ erg s ⁻¹]	$L_{X,max}$ [x10 ²⁹ erg s ⁻¹]
M1	2.40	0.72	1.32	4.84
M2	2.12	0.68	1.61	4.88
M3	1.52	0.53	2.66	5.22

REFERENCES

- Anderson, L. D., Deharveng, L., Zavagno, A., et al. 2015, *ApJ*, 800, 101
- Avedisova, V. S., & Kondratenko, G. I. 1984, *Nauchnye Informatsii*, 56, 59
- Campbell, B. 1984, *ApJ*, 282, L27
- Castellanos-Ramírez A., Rodríguez-González A., Esquivel, A., Toledo-Roy, J. C., Olivares, J., Velázquez, P. F., 2015, *MNRAS*, 450, 2799
- Chu, Y.-H. 2008, *Massive Stars as Cosmic Engines*, 250, 341
- Chu You-Hua 2016 *J. Phys.: Conf. Ser.* 728 032007
- Chu, Y.-H., & Mac Low, M.-M. 1990, *ApJ*, 365, 510
- Chu, Y.-H., Treffers, R. R., & Kwitter, K. B. 1983, *ApJS*, 53, 937
- Chu, Y. H. 1991, *Wolf-Rayet Stars and Interrelations with Other Massive Stars in Galaxies*, 143, 349
- Chu, Y.-H., & Mac Low, M.-M. 1996, *Roentgenstrahlung from the Universe*, 241
- Courtès, G. 1989, *IAU Colloq. 120: Structure and Dynamics of the Interstellar Medium*, 350, 80
- Crowther, P. A. 2007, *ARA&A*, 45, 177
- Deharveng, L., Zavagno, A., Schuller, F., et al. 2009, *A&A*, 496, 177
- Dere, K. P., Landi, E., Mason, H. E., Monsignori, Fossi B. C., Young, P. R., 1997, *A&AS*, 125, 149
- Dyson, J.E., & Williams, D.A. 1980, *The Physics of the Interstellar Medium*, (New York:John Wiley & Sons)
- Esquivel, A., Raga, A. C., Cantó, J., Rodríguez-González, A., López-Cámara, D., Velázquez, P. F., De Colle, F., 2010, *ApJ*, 725, 1466
- Friend, D. B., & Abbott, D. C. 1986, *ApJ*, 311, 701
- García-Díaz, M. T., Henney, W. J., López, J. A., & Doi, T. 2008, *RevMexAA*, 44, 181
- Gvaramadze V. V., Mackey J., Kniazev A. Y., Langer N., Chené A.-N., Castro N., Haworth T. J., & Grebel E. K., 2017, *MNRAS*, 466, 1857
- Georgelin, Y. P., & Georgelin, Y. M. 1970, *A&AS*, 3, 1
- Gosset, E., Nazé, Y., Claeskens, J.-F., et al. 2005, *A&A*, 429, 685
- Gruendl, R. A., Chu, Y.-H., Dunne, B. C., & Points, S. D. 2000, *AJ*, 120, 2670
- Harper-Clark, E., & Murray, N. 2009, *ApJ*, 693, 1696
- Heckathorn, J. N., Bruhweiler, F. C., & Gull, T. R. 1982, *ApJ*, 252, 230
- Landi, E., Del Zanna, G., Young, P. R., et al. 2006, *ApJS*, 162, 261
- Le Coarer, E., Rosado, M., Georgelin, Y., Viale, A., & Goldes, G. 1993, *A&A*, 280, 365
- Mackey, J., Gvaramadze, V. V., Mohamed, S., & Langer, N. 2015, *A&A*, 573, A10
- Mackey J., Haworth T. J., Gvaramadze V. V., Mohamed S., Langer N., Harries T. J., 2016, *A&A*, 586, A114
- Marston, A. P., Yocum, D. R., Garcia-Segura, G., & Chu, Y.-H. 1994, *ApJS*, 95, 151
- Martins, F., Pomarès, M., Deharveng, L., Zavagno, A., & Bouret, J. C. 2010, *A&A*, 510, A32
- McCall, M. L., Rybski, P. M., & Shields, G. A. 1985, *ApJS*, 57, 1
- Miller, G. J., & Chu, Y.-H. 1993, *ApJS*, 85, 137
- Moore, B. D., Hester, J. J., & Scowen, P. A. 2000, *AJ*, 119, 2991

- Oey, M. S. 1996, *ApJ*, 465, 231
- Prinja, R. K., Barlow, M. J., & Howarth, I. D. 1990, *ApJ*, 361, 607
- Raga, A. C., Cantó, J., & Rodríguez, L. F. 2012b, *RMxAA*, 48, 199
- Reyes-Iturbide, J., Rosado, M., Rodríguez-González, A., et al. 2014, *AJ*, 148, 102
- Rodríguez, L. F., Canto, J., & Moran, J. M. 1988, *ApJ*, 333, 801
- Rodríguez-González, A., Velázquez, P. F., Rosado, M., et al. 2011, *ApJ*, 733, 34
- Rogers, H., & Pittard, J. M. 2014, *MNRAS*, 441, 964
- Rosado, M., Langarica, R., Bernal, A., et al. 1995, *Revista Mexicana de Astronomía y Astrofísica Conference Series*, 3, 263
- Russeil, D. 2003, *A&A*, 397, 133
- Sharpless, S. 1959, *ApJS*, 4, 257
- Spitzer, L. 1978, *Physical Processes in the Intestellar Medium* (New York: Wiley Interscience)
- Sternberg, A., Hoffmann, T. L., & Pauldrach, A. W. A. 2003, *ApJ*, 599, 1333
- Tenorio-Tagle, G., 1979, *A&A*, 71, 59.
- Tinoco Arenas, A., González Bolívar, M., Medina Cobarrubias, R., & Raga, A. C. 2015, *RMxAA*, 51, 239
- Toalá, J. A., Guerrero, M. A., Chu, Y.-H., et al. 2016, *MNRAS*, 456, 4305
- Toledo-Roy, J. C., Velázquez, P. F., Esquivel, A., Giacani, E., 2014, *MNRAS*, 437, 898
- Torii, K., Hasegawa, K., Hattori, Y., et al. 2015, *ApJ*, 806, 7
- Toro, E. F., Spruce, M., & Speares, W. 1994, *Shock Waves*, 4, 25
- Valdez-Gutiérrez, M., Rosado, M., Georgiev, L., Borissova, J., & Kurtev, R. 2001, *A&A*, 366, 35
- Weaver, R., McCray, R., Castor, J., Shapiro, P., & Moore, R. 1977, *ApJ*, 218, 377
- Wrigge, M., Chu, Y.-H., Magnier, E. A., & Wendker, H. J. 2005, *ApJ*, 633, 248
- Zavagno, A., Pomarès, M., Deharveng, L., et al. 2007, *A&A*, 472, 835
- Zavagno, A., Russeil, D., Motte, F., et al. 2010, *A&A*, 518, L81
- Zhang, N. -X., Chu, Y. -H., Williams, R. M., et al. 2014, *ApJ*, 792, 58

Full addresses go here